T. Tonegawa[1], E. Araki[1], H. Matsumoto[1], T. Kimura[1], K. Obana[1], G. Fujie[1], R. Arai[1], K. Shiraishi[1], M. Nakano[1], Y. Nakamura[1], T. Yokobiki[1], and S. Kodaira[1]

[1] Japan Agency for Marine-Earth Science and Technology (JAMSTEC), 2-15, Natsushima, Yokosuka Kanagawa, 237-0061, Japan.

Corresponding author: Takashi Tonegawa (tonegawa@jamstec.go.jp)

Key Points:

- *P* waves were extracted from ambient seafloor noise records observed by DAS at a frequency band of 0.1–0.3 Hz and up to a distance of 7 km.
- The extraction of *P* waves depends on weather conditions, and can be perfomed on stormy days.
- The distance in which the P waves emerge is controlled by the *P* incident angle and the DAS sensitivity to apparent velocities.

Abstract

Seismic wave extractions have been performed using ambient noise records observed by distributed acoustic sensing (DAS) technology. Extractions of microseisms can be investigated at a local scale using such DAS records observed in the ocean. Here, we show *P* and Scholte wave extractions from ambient seafloor noise observed by DAS along a submarine cable deployed off Cape Muroto in the Nankai subduction zone, Japan. The *P* waves can be observed at a frequency band of 0.1–0.3 Hz and up to a distance of 6–7 km. The distance in which the *P* waves can be observed is controlled by the *P* incident angle and the DAS sensitivity to the observable apparent velocity. The effective extractions of *P* and Scholte waves are performed in correspondence to large significant wave heights of the sea surface, which indicate that these waves are originated from fluid distturbances at the sea surface.

Plain Language Summary

The density of seismic observations on land is typically higher than those in the ocean. However, higher density observations in both land and ocean regions can be made using the recently developed distributed acoustic sensing (DAS). In this study, we focus on waves persistently propagating in the Earth, which are excited by ocean swell and called microseisms. Ocean swell at the sea surface primarily excites surface waves, but *P* and *S* waves excited by ocean swell, especially during tropical storms, were observed on a global scale. Because this indicates that body waves may be locally excited by sea surface disturbances, we investigate this problem using DAS records. Our results show that large amplitudes of *P* waves were observed when an atmospheric low pressure passed around Japan, and those amplitudes became weak when the significant wave height in the ocean was small. Although many previous studies on global or regional scales have indicated that microseisms are originated from fluid disturbances at the sea surface, this study observed the excitation of *P* and surface waves right beneath the sea surface disturbances.

1 Introduction

Distributed acoustic sensing (DAS) using fiber optic cables is now a powerful tool for detecting signals of various wave propagations, because the station density along a cable is higher than the typical density of seismic observations using individual seismic sensors. For example, DAS on land is capable of observing signals from regional (Lindsey et al. 2017) and teleseismic earthquakes (Yu et al. 2019) and can estimate shallow S-wave velocity (Vs) structure from ambient noise records (Dou et al. 2017; Ajo-Franklin et al. 2019). P wave is also extracted from ambient noise records acquired by downhole DAS on land (Lellouch et al. 2019). DAS in submarine cables can capture seismic waves from earthquakes (Sladen et al. 2019; Lindsey et al. 2020; Lior et al. 2021) and also ocean-specific wavefields, including infragravity waves (Williams et al. 2019) and hydroacoustic waves (Matsumoto et al. 2021).

As with land cases, ambient noise records observed by DAS have recently been used to estimate the seismic velocity structures beneath submarine cables. Previous studies have estimated the Vs structures within sediment layers in the Japan Trench (Spica et al. 2020) and in the Monterey Bay, California (Cheng et al. 2021). These structure estimations are based on the retrieval of surface waves, because DAS-based ambient noise records are dominated by surface waves related to microseisms. However, wave-wave interactions from ocean swells indeed excite P waves (Longuet-Higgins, 1950; Hasselmann, 1963), as they can be observed in global (Gerstoft et al., 2006; Landès et al., 2010; Farra et al., 2016; Gualtieri et al., 2014; Koper et al., 2010; Nishida and Takagi, 2016) and regional (Tonegawa et al. 2021) seismic observations. The teleseismic P waves can be primarily observed at a frequency band of 0.1–0.3 Hz. These observations mean that the ambient noise acquired by the DAS potentially contained P waves that were excited at local scales.

In this study, ambient noise records observed by a submarine cable deployed off Cape Muroto in the Nankai subduction zone, Japan (Fig. 1) are employed to extract P and surface waves. We hereafter refer to the cable as the Muroto cable. Because the ambient noise wavefield in the ocean is closely related to the intensity of ocean swell, we investigate the retrieved waves based on the significant wave height around the cable. The Philippine Sea Plate subducts northwards in the Nankai Trough (Fig. 1), and the accretionary prism is located north of the trough. The Muroto cable was deployed on the soft sediment of the accretionary prism, and ambient noise records observed by the cable are plausibly dominated by surface waves propagating within the prism. In order to investigate the characteristics of the retrieved waves, we estimate the Vs structure within the accretionary prism beneath the Muroto cable using the retrieved Scholte waves: Scholte wave is a surface wave propagating at an interface between solid and fluid, and it seems that the energy of the Scholte wave at frequency < 2 Hz is concentrated on the seafloor, but its amplitude tails extend to both the sea water and marine sediments.

2 Data

The Muroto cable is 128 km long (Fig. 1), of which the cable section from 0.35 km to 2.14 km is buried 0.5-1.0 m beneath the seafloor, but the rest of the cable seawards is unburied and lays on the seafloor with its own weight (Matsumoto et al. 2021). The DAS data was recorded by AP Sensing (model N5200A) over a sensing length of 50 km along the cable, with a gauge length of 40.4 m and a sensor spacing of 5.1 m, in which the differential phase at each channel was measured by the interrogator: the differential phase can be converted to strain. Detailed descriptions of the cable and AP Sensing observations can be found in Matsumoto et al. (2021) and Ide et al. (2021), respectively. The water depth of the cable ranges between 0 and 1,100 m, and topographic relief is present at a cable distance of 30 km from the coastline. The relief continues eastwards to a shallow bank called Tosa-Bae, beneath which a large seamount is subducting (Kodaira et al. 2002). The sampling rate was decimated from 500 Hz to 50 Hz for the processing in this study. Here, we defined Stages A–D by the ranges of significant wave height (SWH) observed off the Cape Muroto, A: $>$ 6 m, B: 3–6 m, C: ~1 m and D: 2–4 m. The periods of data collection were January 27–31, 2020 and February 1–20, 2021, but we used the data for 5 days for the 2020 observation and for periods of Stages C and D for the 2021 observation. The SWH was observed by a Global Positioning System (GPS) buoy (The Nationwide Ocean Wave information network for Ports and HArbourS (NOWPHAS)) (Fig. 1).

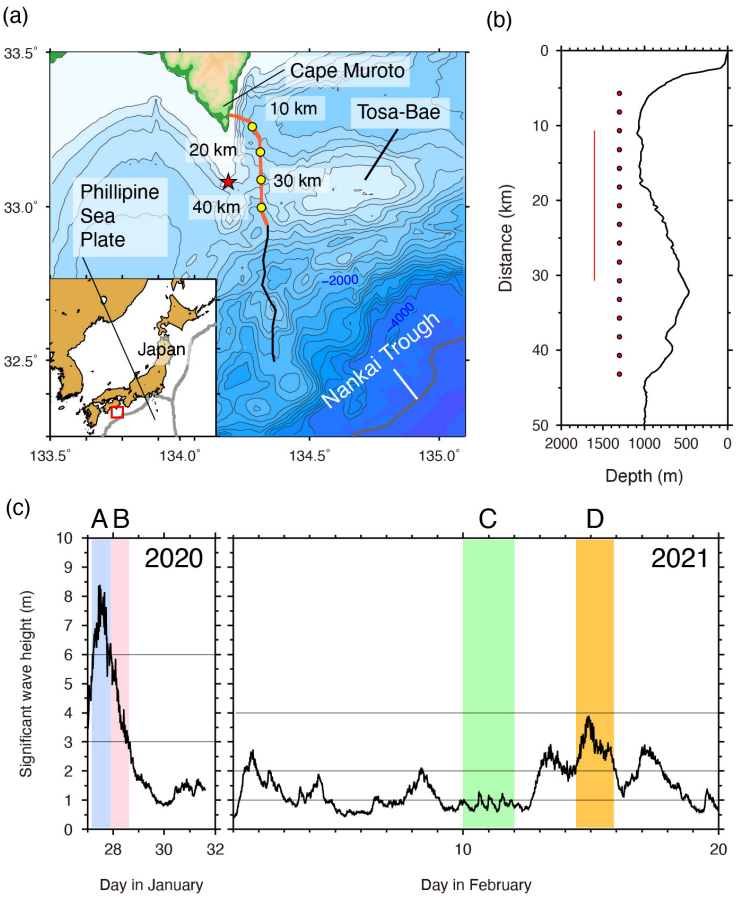

Figure 1. Geometry of the Muroto cable on the seafloor. (a) Black and red lines show the location of the Muroto cable and the section used for the DAS measurements with 10 km increments (yellow circles), respectively. (b) Water depths along the Muroto cable. Red dots and red line represent the reference points and the distance range of the 20-km subarray, respectively. (c) Significant wave height (SWH) observed off the Cape Muroto, indicated by the red star in panel (a). Stages A–D are defined by A: SWH $>$ 6 m, B: SWH = 3–6 m, C: SWH = 1 m and D: SWH = 2–4 m.

3 Methods

3.1 Ambient noise analysis

The space sampling of 5.1 m on the continuous records was decimated to 51 m by stacking the records within a spacing of –20.5 to 25.5 m for each 51 m station (stacking the records of 10 stations). The wavefield may change region-by-region due to variations in the water depth along the cable. To extract the wavefields region-by-region, we divided the cable into 16 subarrays with

reference point increments of 2.5 km, wherein each subarray that had a direct separation distance of 5 km from the reference point to the farthest station was secured. The stations at the cable distances slightly greater than 5 km from the reference points were also used in the subarrays because the cable is not linear (Fig. S1). The reference points along the cable are summarized in Table S1. Moreover, to observe waves with longer wavelengths, we also prepare a subarray with a distance of 20 km for the reference point of subarray 3, and 14 subarrays with a distance of 10 km for the same reference points as those for 5 km. Within each subarray, using the continuous records of the differential phase with a time window of 75 s, cross-correlation functions (CCFs) were calculated using the spectral whitening in the frequency domain (Bensen 2007; Brenguier 2007). The CCFs were stacked over each period of Stages A–D and every day on January 28–31, 2020. Although the space sampling of the CCFs along the cable was resampled to 51 m, the direct separation distances between the two stations were various because the cable was not linear. The CCFs for all station pairs in each subarray were stacked using a 50 m spatial bin. Figures 2a and b shows that the obtained wavefield at a frequency of 0.4–0.8 Hz is the Scholte waves with a propagation velocity of < 1.0 km/s (first higher and fundamental modes).

On the other hand, waves with higher apparent velocities can also be observed at 0.1–0.3 Hz in the 20-km subarray (arrows in Fig. 2c) and in the 10-km subarrays (Fig. S2). The positive amplitudes at a zero lag time at separation distances of two stations (L) greater than 8 km are caused by the instrumental noise. Figure 2d shows the peak traces of the maximum amplitudes of the waves observed at the subarrays 1–14, in which the amplitudes in the positive and negative lag times are stacked. Their apparent velocitites are around 1.5 km/s and 4 km/s at L = 1.5–4 km and L $>$ 4 km, respectively. Based on the apparent velocities, we consider that the waves emerged at L 4 km and L $<$ 4 km are *P* wave and the contamination of *P* and Scholte waves. At L $<$ 4 km, the travel times of the waves in the northern part of the cable (warm colors) tended to be slower than those in the southern part (cool colors). In the subsequent section, to confirm the velocity structure beneath the cable and compare it with the observed travel times, we estimate the *Vs* structure using the dispersion curves of the Scholte waves.

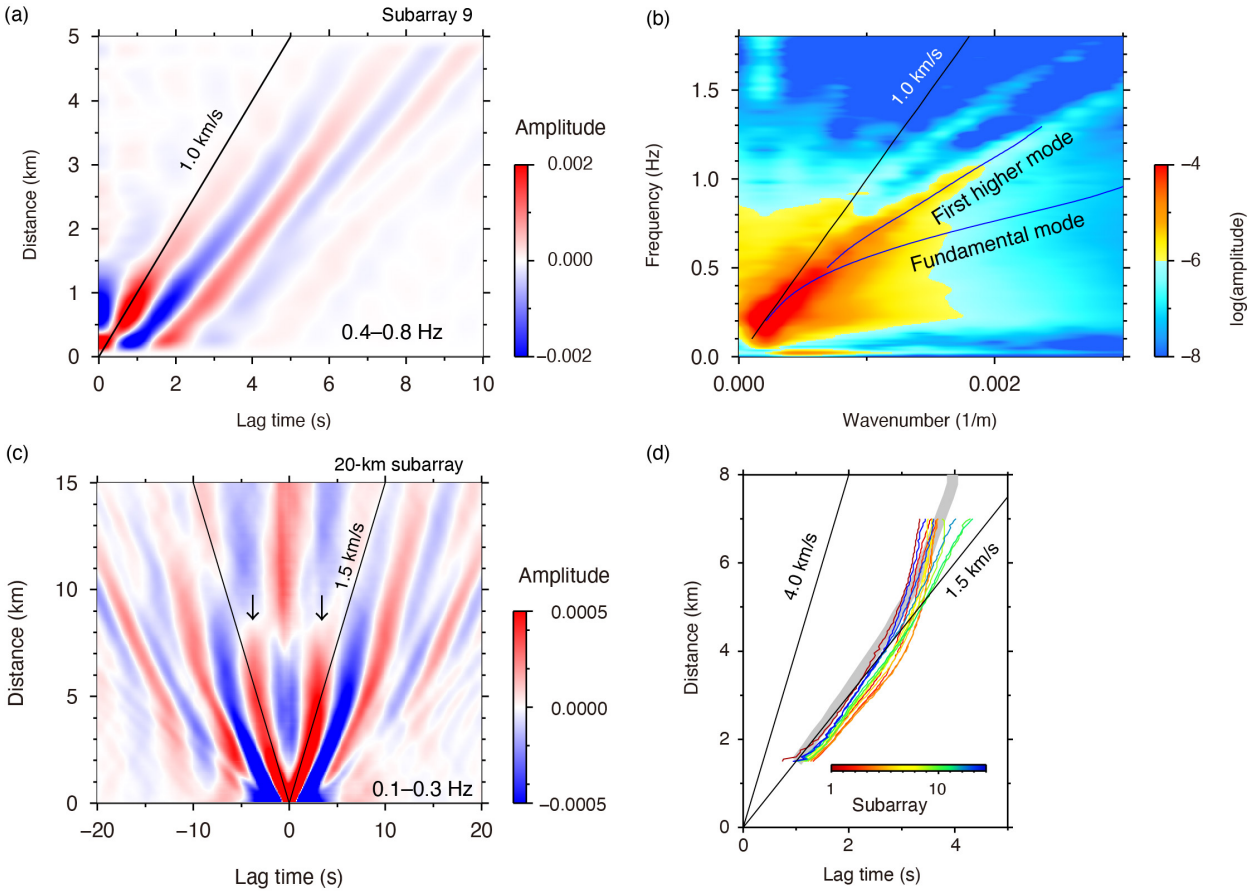

Figure 2. Cross-correlation functions (CCFs) s in the time-distance and *f*-*k* domains for subarray 9 for Stage A. (a) CCFs at 0.4–0.8 Hz aligned as a function of the separation distance between two stations. Positive lag time indicates the wave propagation northward along the cable. The line shows the reference propagation velocity of 1.0 km/s. (b) CCFs in the *f*-*k* domain with (blue lines) the picked dispersion curves (c) CCFs at 0.1–0.3 Hz with the reference velocity of 1.5 km/s for the 20-km subarray for Stage A. Positive and negative lag times indicate the wave propagations northwards and southwards along the cable, respectively. (d) The travel time curves of the *P* waves for the 10-km subarrays (Fig. S2) with the reference velocities of 1.5 and 4.0 km/s. The gray line indicates the theoretical travel time curve of the *P* wave.

3.2 FK analysis of Scholte waves

We applied the Fourier transform to the one-day CCF dataset from each subarray to obtain the CCFs in the *f*-*k* domain (Fig. 2b). To obtain the dispersion curves of the fundamental and first higher modes of the Scholte wave, the maximum amplitudes at each frequency between 0.2 and 1.0 Hz and between 0.5

and 1.3 Hz were searched within a phase velocity range of 200–1200 m/s and 700 and 1500 m/s in the *f-k* domain, respectively (Fig. S3), but these search ranges were slightly changed by the velocities of the dispersion curves at each subarray. Here, for some subarrays, because the dispersion curves of the higher and lower frequency sides of the frequency range were unstable, we limited the frequency bands at the stations for velocity estimations: these are summarized in Table S1.

3.3 Vs profile estimation

For each subarray, we estimated the one-dimensional (1D) *Vs* model with the dispersion curve of the Scholte wave using a non-linear inversion, simulated annealing. Simulated annealing is a Monte Carlo method that searches the global minimum by lowering the possibility of the acceptance of random perturbations to the model parameters with decreasing temperature (e.g. Chevrot 2002). The misfit function is described as

$$E = \sum_{i=1}^{M} \left| c_{\mathrm{obs}}\left(f_i\right) - c_{\mathrm{syn}}(f_i) \right| + \sum_{j=1}^{N} \left| d_{\mathrm{obs}}\left(f_j\right) - d_{\mathrm{syn}}(f_j) \right| \quad (1),$$

where $c_{obs}(f_i)$ and $c_{syn}(f_i)$ are the observed and predicted phase velocities, respectively, for the i-th frequency ($i = 1 \cdots M$) for the fundamental mode, and $d_{obs}(f_j)$ and $d_{syn}(f_j)$ for the j-th frequency ($j = 1 \cdots N$) correspond to the first higher mode.. The predicted phase velocity was calculated using DISPER80 (Saito 1988). A 1D *Vs* model averaged over all the 1D *Vs* models beneath the seafloor obtained for the Nankai subduction zone (Tonegawa et al. 2017) was selected as the initial *Vs* model, and *Vs* in the sea water was set to be zero. The *Vp* and density models were converted from *Vs* using empirical relationships (Brocher, 2005).

The update of v_k is based on a previous study (Tonegawa et al. 2017), where v_k is the 1D *Vs* profile at the k-th layer. At each iteration step, we perturbed v_k by a depth interval of 0.1 km using random numbers, referring to a previous study (Chevrot 2002). The updated v_k' is described as

$$v_k^{'} = \begin{cases} v_k - v & if\ \alpha < 0.5 \\ v_k + v & if\ \alpha > 0.5 \end{cases} \quad (2),$$

where is a random number between 0 and 1. The velocity perturbation is Δv = 0.02 km s^{-1}. The minimum perturbed velocity was set as 0.4 km s^{-1}. Similar to the previous study (Tonegawa et al. 2017), the maximum velocity gradients above and below 2 km beneath the seafloor were set as 2.0 s^{-1} and 1.0 s^{-1}, respectively. The updated v_k' is accepted when ΔE 0, where ΔE is the difference between E and that of the previous iteration. If ΔE 0, the acceptance depends on the probability,

$$P = \exp\left(-\frac{E}{T}\right) \quad (3),$$

where T is the temperature. The annealing schedule at the n-th step can be written as $T_n =$ $^{n}T_0$, and we set = 0.996 and $T_0 = 3E_0$, where E_0 is the result of the first step of the estimation E. If a random number between 0 and

1, , is less than P, the updated v_k' is accepted. The Vp and density models are also updated using the empirical relationships after the acceptance of v_k'. The total number of iteration is 2000. In order to estimate the error of the Vs profile at each subarray, we prepared 30 profiles of v_k' with changing random number seeds for the inversion, and estimated the standard deviations from the obtained profiles.

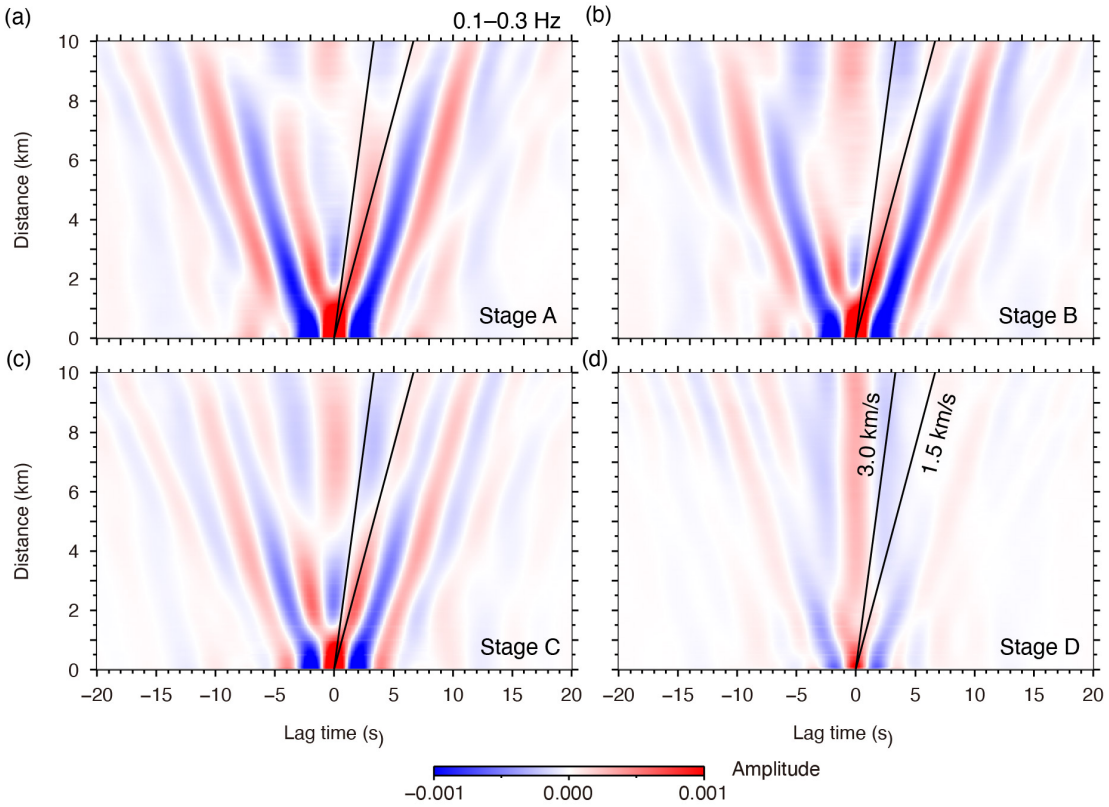

Figure 3. CCFs at 0.1–0.3 Hz for the 10-km subarray 9 for (a) Stage A, (b) Stage B, (c) Stage D, and (d) Stage C, with the reference velocities of 1.5 and 3.0 km/s. Positive and negative lag times indicate the wave propagations northward and southward along the cable, respectively.

4 Results

Figure 3 displays the stacked CCFs at the 10-km subarray 9 from stormy to calm conditions in the ocean (Stages A–D). The P waves reaches to a distance of 6–7 km at stormy days (Stage A), but the distance at which the P waves appear tends to be short with decreasing SWH (Stages B and C), and those amplitudes disappeared at Stage D. Such weak wave propagations under calm conditions result in the emergence of the instrumental noise at a zero lag time. This observation indicates that the origin of the P and surface waves is presumably

located at the sea surface.

Moreover, various surface wave modes followed by the *P* waves can also be observed (Fig. 2c). These modes are also excited by ocean swell, and the amplitudes of the waves tend to be small according to the SWH as well as the *P* waves. This feature can be clearly seen in the CCFs for the 20-km subarrays for Stages A and D (Figs. S4a and S4b), in which only surface waves propagating southward are dominant under calm condition (Fig. S4b). The features that (1) the P waves reaches to L = 6–7 km and (2) surface waves propagate at longer distances can be seen in the CCFs at 0.2–0.5 Hz (Fig. S4c), while large amplitudes from the instrumental noise are dominant around a zero lag time at 0.07–0.1 Hz (Fig. S4d).

Figure 4a shows the 1D *Vs* structures for the 16 subarrays along the cable for Stage A, in which the following two features were identified. (1) A shallow high velocity region is present, and its peak is located slightly south of the seafloor topographic high. This may be related to the deformation of the accretionary prism due to the subducting seamount. (2) The shallow *Vs* values are relatively high and low in the ridge and basin regions, respectively. The errors of the *Vs* profiles are sufficiently small to observe the above two features (Fig. 4b). Moreover, features (1) and (2) are enhanced in the *Vs* perturbation profiles (Fig. S5), in which the perturbations were estimated with the reference profile averaged over the 16 *Vs* profiles beneath the seafloor.

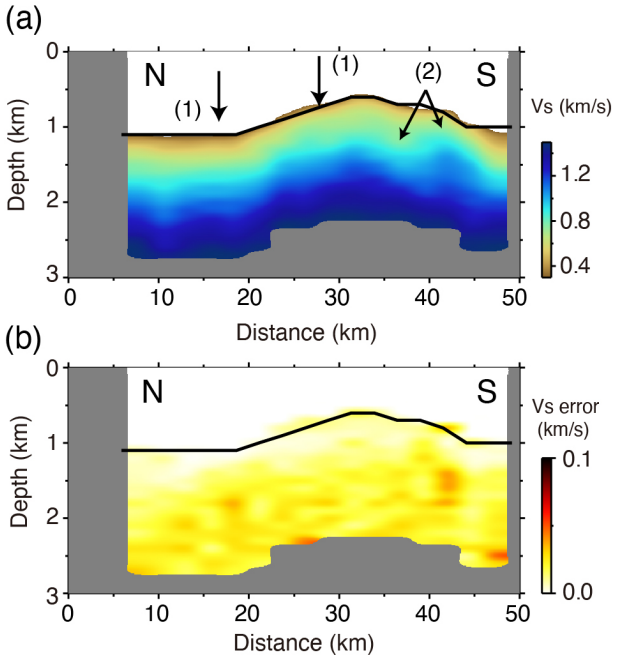

Figure 4. Seismic velocity profiles along the Muroto cable. (a) *Vs* profiles along the cable, created using the CCFs for Stage A. Specific features (1)–(2) are

observed (see detailed in the text). (b) Error for panel (a).

5 Discussion

5.1 *P* wave extraction and weather conditions

In this section, we confirm whether the waves with apparent velocity of 4.0 km/s are *P* waves excited by ocean swell by investigating the travel time, apparent velocity and incident angle. We calculated the travel time of *P* wave using the reference *Vp* model used in the section 3.3 (Fig. S6) to reproduce the feature of the observed travel time curves, particularly for the part of the gradient change of the travel time curve at L = 4 km (Fig. 2d). However, the calculated travel times were slightly faster than the observed ones. We therefore slightly reduced the shallow *Vp* values (Fig. S6a) with trial and error, and then reproduced the feature of the observed one. This means that, although the velocity structure may be slower than the reference *Vp* model, the observed travel time curve can be reproduced with the appropriate *Vp* model.

However, the travel time at L = 1.5–4.0 km is slightly delayed from the reference velocity of 1.5 km/s. To investigate the wavefield excited by a vertical force at the sea surface, we conducted a simple 2D numerical simulation with a water depth of 1 km and the reduced *Vp* model beneath the seafloor (See details in Text S1 and Figs. S7). As a result, large amplitudes of surface waves slightly slower than 1.5 km/s were synthesized in the horizontal component (Figs. S7b and S7d). It is considered that such surface waves are dominant in the ambient wavefield during stormy condition, and that the waves in the observed CCFs at the distance range consist of both *P* and surface waves. Moreover, the numerical simulation results show that the propagation velocities of surface waves slower than 1.5 km/s depend on *Vs* at shallow depths (e.g., 'C' in Figs. S7b and S7d). Figure 4a shows that the relatively slow and fast velocities at the shallow depths in the northern and southern parts of the cable. These results indicate that the observed travel time difference (L $<$ 4 km in Fig. 2d) reflects the shallow velocity difference between the northern and southern subarrays. Furthermore, although the apparent velocities of the *P* waves at L $>$ 4 km become faster seawards (green to blue lines in Fig. 2d), those at subarrays 1–7 are also fast (yellow to red lines in Fig. 2d). Because the bottom depth of the diving *P* wave reaches to 2.6 km from the seafloor with the reduced *Vp* model, the fast apparent velocity may refect the deeper structure that is extended from land than the obtained Vs profile.

The other points for considering the *P* wave extraction are the distance range and incident angle of the observed *P* wave. We found that the maximum distance that a *P* wave reaches is roughly ~6–7 km (Fig. 1c), which indicates that the raypath of the *P* wave to the seafloor has a larger incident angle, measured from vertically downward, than those with greater offsets. Using the reduced *Vp* model (Fig. S6a), the incident angle of *P* wave changes from 60^{o} at L = 2–3 km to 30^{o} at L = 6 km (Fig. S6b), which indicate that the ray path of the *P* waves within L 6 km reaches the cable with a larger angle than 30^{o} from vertically

downward. For the DAS observation, the *P* wave extractions are related to the strain of the *P* wavefield observed in the horizontal plane. The ambient noise records observed by DAS almost represent the horizontal component of seafloor motion, which unables us to observe *P* waves with near-vertical incidences to the seafloor (close to 0º measured from vertically downward). However, in our case, observable amplitudes of the *P* wave can be projected onto the horizontal plane due to a large incident angle of the *P* wave to the seafloor (Fig. S6d). This feature is also confirmed by the numerical simulation (Text S1).

In addition to the incident angle effect, the disappearance of the *P* wave at L = 6–7 km may have been caused by a lack of the fast apparent velocity in the DAS observation. Because amplitudes of signals are reduced with increasing apparent velocities (Lior et al. 2021), the amplitudes with apparent velocities of faster than 4 km/s may not be observed by the cable.

Based on the above observations and simulations, the waves that we observed at L = 4–7 km are *P* waves excited at a local scale, and we consider that *P*-wave extraction quality is attributed to the weather conditions in the observation period. An atmospheric low pressure system passed near Japan on January 27 affecting the intensity of the ocean swell until January 28. The *P* wave extractions in this study were performed at frequencies of 0.1–0.3 Hz (Fig. 2c), which are within the typical frequency range at which teleseismic *P* waves excited by atmospheric low pressure are observed at a global scale. The amplitudes of *P* and surface waves responding to the SWHs in our results indicate that those waves were effectively excited on stormy days. Therefore, our observations indicate that *P* waves are originated from ocean swell at the sea surface, and that the *P* wave retrievals depend on weather conditions.

5.2 Stability of the obtained velocity profiles

In contrast to *P* waves, the Scholte wave amplitudes were retrieved in the CCFs even under calm conditions at frequencies higher than ~0.3 Hz. In order to evaluate the stability of the obtained *Vs* profiles, we created profiles for 4 days in January 28–31, 2020 (Fig. S8). The results for these days reproduced the features (1)–(2) shown in Fig. 4a. The *Vs* values were stable and fluctuated by less than ~0.06 km/s and less than 0.03 km/s at depths shallower than 0.5 km below the seafloor. If a large temporal change in *Vs* occurrs (due to a large earthquake), it may be possible to monitor its variations at shallow depths.

6 Conclusions

We extracted *P* waves from ambient seafloor noise observed by DAS, and the identification of the *P* waves are based on the distance for which the *P* waves can be observed as well as their incident angle. Moreover, we estimated the shallow *Vs* structure along the cable, and the travel times of the extracted *P* and Scholte waves correspond to the lateral variation of the estimated *Vs* structure. By comparing the SWHs with the wavefield emerged in the CCFs, we found that *P* wave extractions depend on weather conditions and can be accomplished on stormy days. Previous global or regional scale studies have

reported that microseisms are originated by fluid disturbances at the sea surface, but this study observed the excitation of P and surface waves right beneath the sea surface disturbances. Although the wavefield was compared to a maximum SWH of 6–8 m in this study, the investigation of extracted waves with larger SWHs and longer durations may help to further understand the excitation of microseisms including body waves. In addition, because the *Vs* profiles obtained using the one-day CCFs were stable, we expect that the subseafloor structures along the Muroto cable can be monitored if the observation periods can be extended.

Acknowledgments, Samples, and Data

We used significant wave height data provided by The Nationwide Ocean Wave information network for Ports and HArbourS (NOWPHAS) (https://www.mlit.go.jp/kowan/nowphas/index_eng.html).

Data Availability Statement

The data that is used for reproducing all the figures are available online (Zenodo: doi:10.5281/zenodo.5574799).

References

Ajo-Franklin, J. B., Dou, S., Lindsey, N. J., Monga, I., Tracy, C., Robertson, M., et al. (2019). Distributed Acoustic Sensing Using Dark Fiber for Near-Surface Characterization and Broadband Seismic Event Detection. *Scientific Reports*, *9*, 1328. https://doi.org/10.1038/s41598-018-36675-8

Bensen, G. D., Ritzwoller, M. H., Barmin, M. P., Levshin, A. L., Lin, F., Moschetti, M. P., et al. (2007). Processing seismic ambient noise data to obtain reliable broad-band surface wave dispersion measurements. *Geophysical Journal International*, *169*(3), 1239–1260. https://doi.org/10.1111/j.1365-246X.2007.03374.x

Brenguier, F., Shapiro, N. M., Campillo, M., Nercessian, A., & Ferrazzini, V. (2007). 3-D surface wave tomography of the Piton de la Fournaise volcano using seismic noise correlations. *Geophysical Research Letters*, *34*(2), 1351–5. https://doi.org/10.1029/2006GL028586

Brocher, T. M. (2005). Empirical Relations between Elastic Wavespeeds and Density in the Earth's Crust. *Bulletin of the Seismological Society of America*, *95*(6), 2081–2092. https://doi.org/10.1785/0120050077

Cheng, F., Chi, B., Lindsey, N. J., Dawe, T. C., & Ajo-Franklin, J. B. (2021). Utilizing distributed acoustic sensing and ocean bottom fiber optic cables for submarine structural characterization. *Scientific Reports*, *11*, 1–14. https://doi.org/10.1038/s41598-021-84845-y

Chevrot, S. (2002). Optimal measurement of relative and absolute delay times by simulated annealing. *Geophysical Journal International*, *151*, 164–171.

Dou, S., Lindsey, N., Wagner, A. M., Daley, T. M., Freifeld, B., Robertson, M., et al. (2017). Distributed Acoustic Sensing for Seismic Monitoring of The Near Surface: A Traffic-Noise Interferometry Case Study. *Scientific Reports*, *7*, 11620. https://doi.org/10.1038/s41598-017-11986-4

Farra, V., Stutzmann, E., Gualtieri, L., Schimmel, M., & Ardhuin, F. (2016). Ray-theoretical modeling of secondary microseism Pwaves. *Geophysical Journal International* 206, 1730–1739. https:/doi.org/10.1093/gji/ggw242.

Gerstoft, P., Fehler, M. C., & Sabra, K. G. (2006). When Katrina hit California. *Geophys. Res. Lett.* 33, Q04009–6. https://doi.org/10.1029/2006GL027270.

Gualtieri, L., Stutzmann, E., Farra, V., Capdeville, Y., Schimmel, M., Ardhuin, F., et al. (2014). Modelling the ocean site effect on seismic noise body waves. *Geophysical Journal International* 197, 1096–1106. https:/doi.org/10.1093/gji/ggu042.

Hasselmann, K. (1963). A Statistical Analysis of the Generation of Microseisms. *Review of Geophysics* 1, 177–210.

Ide, S., Araki, E., & Matsumoto, H. (2021). Very broadband strain-rate measurements along a submarine fiber-optic cable off Cape Muroto, Nankai subduction zone, Japan. *Earth, Planets and Space*, *73*, 1–10. https://doi.org/10.1186/s40623-021-01385-5

Kodaira, S., Kurashimo, E., Park, J.-O., Takahashi, N., Nakanishi, A., Miura, S. et al. (2002). Structural factors controlling the rupture process of a megathrust earthquake at the Nankai trough seismogenic zone, *J. Geophys. Res.*, **149**, 815–835.

Koper, K. D., Seats, K., & Benz, H. (2010). On the Composition of Earth's Short-Period Seismic Noise Field. *Bulletin of the Seismological Society of America* 100, 606–617. https://doi.org/10.1785/0120090120.

Landès, M., Hubans, F., Shapiro, N. M., Paul, A., & Campillo, M. (2010). Origin of deep ocean microseisms by using teleseismic body waves. *J. Geophys. Res.* 115, 672–14. https://doi.org/10.1029/2009JB006918.

Lellouch, A., Yuan, S., Spica, Z., Biondi, B., & Ellsworth, W. L. (2019) Seismic velocity estimation using passive downhole distributred acoustic sensing records: Examples from the San Andreas Fault Observatory at Depth, *J. Geophys. Res.*, 124, 6931-6948.

https://doi.org/10.1029/2019JB017533.

Lindsey, N. J., Martin, E. R., Dreger, D. S., Freifeld, B., Cole, S., James, S., et al. (2017). Fiber-Optic Network Observations of Earthquake Wavefields. *Geophysical Research Letters*, *44*, 11792–11799. https://doi.org/10.1002/2017GL075722

Lior, I., Sladen, A., Rivet, D., Ampuero, J.-P., Hello, Y., Lamare, P., et al. (2021). On the Detection Capabilities of Underwater Distributed Acous-

tic Sensing. *Journal of Geophysical Research*, *126*(3), e2020JB020925. https://doi.org/10.1002/essoar.10504330.1

Longuet-Higgins, M. S. (1950). A theory of the origin of microseisms. *Philosophical Transactions of the Royal Society of London. Series a, Mathematical and Physical Sciences*, *243*(857), 1–35.

Matsumoto, H., Araki, E., Kimura, T., Fujie, G., Shiraishi, K., Tonegawa, T., et al. (2021). Detection of hydroacoustic signals on a fiber-optic submarine cable, 1–12. https://doi.org/10.1038/s41598-021-82093-8

Nishida, K., & Takagi, R. (2016). Teleseismic S wave microseisms. *Science* 353, 919–921. https:/doi.org/10.1038/nphys3711.

Saito, M. (1988). DISPER80: a subroutine package for the calculation of seismic normal-mode solutions, in Seismological Algorithms -computational methods and computer programs, p. 469, ed. Doornbos D.J., Academic Press, London, 293–319.

Sladen, A., Rivet, D., Ampuero, J. P., De Barros, L., Hello, Y., Calbris, G., & Lamare, P. (2019). Distributed sensing of earthquakes and ocean-solid Earth interactions on seafloor telecom cables. *Nature Communications*, *10*, 5777. https://doi.org/10.1038/s41467-019-13793-z

Spica, Z. J., Nishida, K., Akuhara, T., Pétrélis, F., Shinohara, M., & Yamada, T. (2020). Marine Sediment Characterized by Ocean-Bottom Fiber-Optic Seismology. *Geophysical Research Letters*, *47*, e2020GL088360. https://doi.org/10.1029/2020GL088360

Tonegawa, T., Araki, E., Kimura, T., Nakamura, T., Nakano, M., & Suzuki, K. (2017). Sporadic low-velocity volumes spatially correlate with shallow very low frequency earthquake clusters. *Nature Communications*, *8*(1), 2048. https://doi.org/10.1038/s41467-017-02276-8

Tonegawa, T., Kimura, T., & Araki, E. (2021). Near-Field Body-Wave Extraction From Ambient Seafloor Noise in the Nankai Subduction Zone. *Frontiers in Earth Science*, *8*, 1–12. https://doi.org/10.3389/feart.2020.610993

Williams, E. F., Fernández-Ruiz, M. R., Magalhaes, R., Vanthillo, R., Zhan, Z., González-Herráez, M., & Martins, H. F. (2019). Distributed sensing of microseisms and teleseisms with submarine dark fibers. *Nature Communications*, *10*, 5778. https://doi.org/10.1038/s41467-019-13262-7

Yu, C., Zhan, Z., Lindsey, N. J., Ajo-Franklin, J. B., & Robertson, M. (2019). The Potential of DAS in Teleseismic Studies: Insights From the Goldstone Experiment. *Geophysical Research Letters*, *46*, 1320–1328. https://doi.org/10.1029/2018GL081195

Figure 1. Geometry of the Muroto cable on the seafloor. (a) Black and red lines show the location of the Muroto cable and the section used for the DAS measurements with 10 km increments (yellow circles), respectively. (b) Water

depths along the Muroto cable. Red dots and red line represent the reference points and the distance range of the 20-km subarray, respectively. (c) Significant wave height (SWH) observed off the Cape Muroto, indicated by the red star in panel (a). Stages A–D are defined by A: SWH $>$ 6 m, B: SWH = 3–6 m, C: SWH = 1 m and D: SWH = 2–4 m.

Figure 2. Cross-correlation functions (CCFs) s in the time-distance and *f*-*k* domains for subarray 9 for Stage A. (a) CCFs at 0.4–0.8 Hz aligned as a function of the separation distance between two stations. Positive lag time indicates the wave propagation northward along the cable. The line shows the reference propagation velocity of 1.0 km/s. (b) CCFs in the *f*-*k* domain with (blue lines) the picked dispersion curves (c) CCFs at 0.1–0.3 Hz with the reference velocity of 1.5 km/s for the 20-km subarray for Stage A. Positive and negative lag times indicate the wave propagations northwards and southwards along the cable, respectively. (d) The travel time curves of the *P* waves for the 10-km subarrays (Fig. S2) with the reference velocities of 1.5 and 4.0 km/s. The gray line indicates the theoretical travel time curve of the *P* wave.

Figure 3. CCFs at 0.1–0.3 Hz for the 10-km subarray 9 for (a) Stage A, (b) Stage B, (c) Stage D, and (d) Stage C, with the reference velocities of 1.5 and 3.0 km/s. Positive and negative lag times indicate the wave propagations northward and southward along the cable, respectively.

Figure 4. Seismic velocity profiles along the Muroto cable. (a) *Vs* profiles along the cable, created using the CCFs for Stage A. Specific features (1)–(2) are observed (see detailed in the text). (b) Error for panel (a).